

Experimental and numerical investigation of standing-wave thermoacoustic instability under transcritical temperature conditions

Ariana Martinez,^{1,a)} Mario Tindaro Migliorino,^{2,b)} Carlo Scalo,^{2,c)} and Stephen D. Heister¹

¹School of Aeronautics and Astronautics, Purdue University, West Lafayette, Indiana 47907, USA

²School of Mechanical Engineering, Purdue University, West Lafayette, Indiana 47907, USA

ABSTRACT:

This manuscript describes an experimental and numerical investigation of transcritical thermoacoustic instability in a standing-wave setup using the refrigerant octafluoropropane (R-218) as the working fluid. Thermoacoustic instability is excited by two microtube heat exchangers separated by a vacuum-jacketed microtube stack. R-218 is allowed to flow axially through the microtubes into a closed resonator while heating and cooling fluids flow radially over the microtubes to create a temperature gradient. The fluid achieved pressure amplitudes up to 669 kPa (97 psi) at a temperature difference $\Delta T = T_{\text{hot}} - T_{\text{cold}}$ of 150 K and a base pressure, P_0 , of 1.3 times the critical pressure (3.43 MPa). The high pressure amplitudes obtained are attributed to the strong density variations near the critical point of the working fluid. The thermoacoustic response was characterized in a set of parametric studies in which ΔT , base pressure, and resonator length were varied. A modeling approach based on linearized Navier–Stokes equations reproduces the experimental results with fair agreement. This work demonstrates promising application of transcritical working fluids to thermoacoustic engines as devices for energy extraction and waste heat removal.

© 2021 Acoustical Society of America. <https://doi.org/10.1121/10.0006659>

(Received 27 May 2021; revised 7 September 2021; accepted 17 September 2021; published online 19 October 2021)

[Editor: Julian D Maynard]

Pages: 2900–2911

I. INTRODUCTION

Thermoacoustic instabilities occur when the coupling between pressure and heat release fluctuations yields acoustic wave amplification (Rayleigh, 1878). These instabilities present challenges in many systems, ranging from hardware damage in jet engine fuel lines (Hunt and Heister, 2017), to uneven combustion fields in liquid rocket engines. However, these physics can also be exploited, permitting the development of thermoacoustic engines (TAEs). TAEs are advantageous because they are able to utilize low-grade heat, or waste heat, to produce acoustic work without moving parts (Jin *et al.*, 2015; Swift, 1988). This provides a unique opportunity for energy recycling and recovery in large systems where even the smallest fraction of energy losses can result in several thousand watts of waste heat. In addition, TAEs can also be used to protect systems in cases where energy losses can cause the system to overheat.

TAEs rely on a Brayton-like thermodynamic cycle where a working fluid exchanges heat nearly isobarically, and, driven by the acoustics, experiences adiabatic expansions and contractions (Swift, 1988). In TAEs, this process is usually instigated by imposing an external temperature

differential on a compact region of the device (known as the thermoacoustic stack).

Significant strides in the development of thermoacoustic engines (Adeff *et al.*, 1991; Backhaus and Swift, 1999, 2000; Ceperley, 1979; Migliori and Swift, 1988; Tijani and Spoelstra, 2011; Yazaki *et al.*, 1998) have led to the fundamental understanding of the conversion of thermal to acoustic power for energy exploitation. The power output of a TAE relies on two fundamental properties of the working fluid: its thermal expansion, α_p , and its thermal diffusion, α_{th} [Eqs. (1)–(2)]:

$$\alpha_p = -\left(\frac{1}{\rho}\right) \frac{\partial \rho}{\partial T}, \quad (1)$$

$$\alpha_{th} = \frac{k}{\rho C_p}. \quad (2)$$

In these equations, ρ is fluid density, T is temperature, k is thermal conductivity, and C_p is specific heat capacity.

The vast majority of studies conducted to exploit thermoacoustic phenomena have utilized working fluids such as air, helium, nitrogen, carbon dioxide, argon, or some combination of these fluids (Dong *et al.*, 2019; Li *et al.*, 2014). This can be attributed to their low Prandtl number and high ratio of specific heats, leading to a more efficient thermal diffusion (Belcher *et al.*, 1999).

However, the thermal expansion coefficient of these ideal gases is relatively low compared to a nonideal fluid

^{a)}Electronic mail: marti730@purdue.edu, ORCID: 0000-0002-1220-759X.

^{b)}Present address: Department of Mechanical and Aerospace Engineering, Sapienza University of Rome, 00184 Rome, Italy, ORCID: 0000-0001-7826-1372.

^{c)}ORCID: 0000-0002-6774-2207.

undergoing phase change or transition through the critical state [Fig. 1(a)]. Thus, the utilization of transcritical fluids offers promise for high thermoacoustic gain due to dramatic density changes when crossing the transcritical region [Fig. 1(b)] (Migliorino and Scalo, 2020b; Swift, 1988). In addition, base density, ρ_0 , plays a crucial role in electric power output capability as massflow directly scales with fluid density. The working fluid used in the present study is the refrigerant octafluoropropane (R-218). As R-218 will have a base density three orders of magnitude larger than ideal gases, TAEs utilizing this fluid would have much larger massflows to exploit.

Nevertheless, the high pressures involved in the handling of transcritical fluids, together with the drop of their thermal diffusivity (hence requiring very small pore size in the heat exchangers and stack), has limited their use in a thermoacoustic engine only to the work of Alexander *et al.* (2018); Alexander *et al.* (2018), who used R-218 as the working fluid. Alexander *et al.* (2018) used a standing wave configuration with a heating element at one end and no cooling element. It was demonstrated that R-218 produced a thermoacoustic response in the range of 5 Hz, which has not been demonstrated in thermoacoustic experiments of any

other working fluid, as typical operation is in the range of tens to hundreds of Hertz.

This outcome has implications for what type of energy extraction device may be used in a thermoacoustic engine, as a low frequency response may be more suitable for devices such as a bi-directional turbine, as is used in the work of de Blok *et al.* (2014). Other known exceptions to the use of ideal gases have been from experiments using liquid sodium (Migliori and Swift, 1988) and liquid water (Malone, 1931) in the subcritical region. Additionally, “wet” thermoacoustic devices have been studied, in which the stack is wetted with water. The vaporization and condensation of the water in the stack acts to reduce the required temperature differences to incite thermoacoustic instabilities (Slaton *et al.*, 2001).

The liquid sodium test apparatus constructed by Migliori and Swift (1988) utilized a standing wave thermoacoustic device similar to the one used in the current study. Heating and cooling fluids were flowed through two heat exchangers on either end of a stack, and acoustic pressure amplitude was measured. The base pressure in the sodium apparatus was 97 bar, and achieved pressure amplitudes as high as 5.4 MPa (783 psi) at a ΔT of 360 K and hot side heat input of 990 W. This is a much higher pressure amplitude

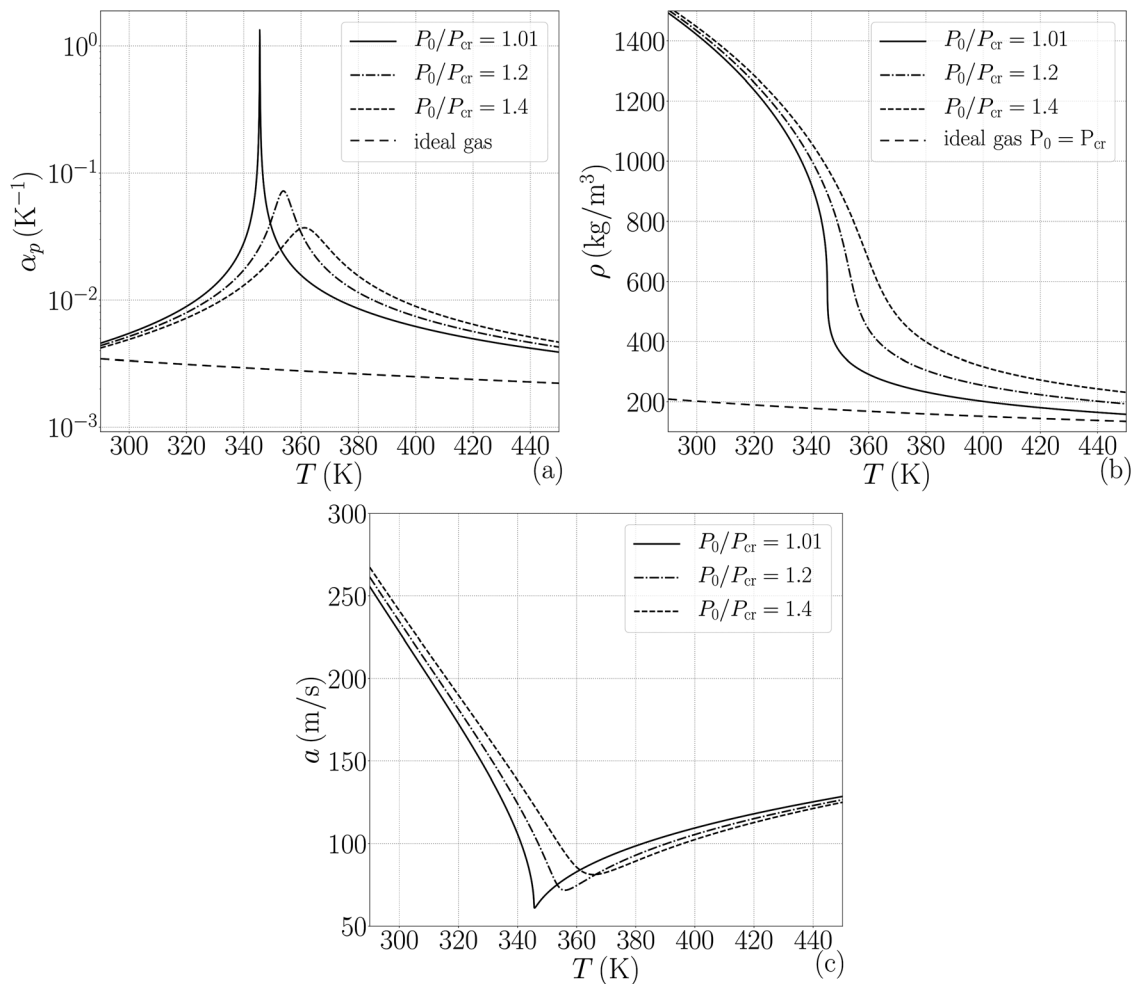


FIG. 1. Isobaric thermal expansion coefficient (a), density (b), and sound speed (c) for R-218 at supercritical pressures computed with the Peng–Robinson equation of state (Peng and Robinson, 1976).

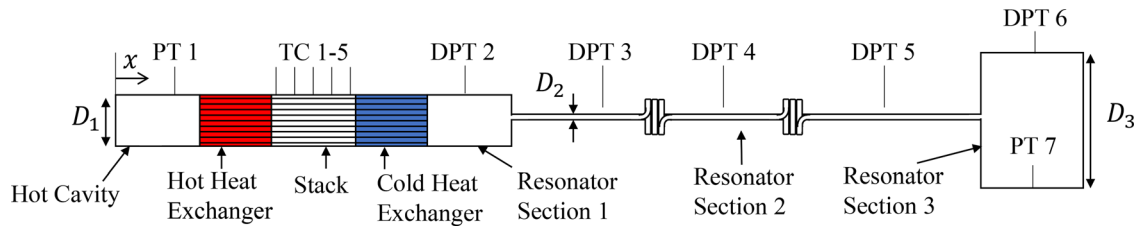


FIG. 2. (Color online) Geometrical setup of the thermoacoustic device. Location on instrumentation is labeled with “PT” for absolute pressure transducer, “DPT” for differential pressure transducer, and “TC” for thermocouple.

than what was achieved in the current study, but at a much higher ΔT requirement as well. At ΔT s less than 300 K, no thermoacoustic instabilities were observed. Additionally, the highly reactive and hazardous nature of sodium makes the use of this working fluid in a practical system difficult.

The experimental study detailed in this manuscript has characterized the thermoacoustic response of R-218 in its transcritical region. R-218 was selected due to its critical properties ($T_{cr} = 345$ K, $P_{cr} = 2.64$ MPa (Lemmon *et al.*, 2016), which are achievable in a laboratory setting and applicable to a number of practical environments (Alexander, 2018; Alexander *et al.*, 2018). A standing-wave thermoacoustic device has been constructed, which contains a bundle of microtubes as the stack, along with a hot heat exchanger (HHX) and cold heat exchanger (CHX) to deliver and remove heat from the working fluid.

This manuscript is organized as follows. First, the design of the thermoacoustic device, the experimental facility, and testing methods are detailed in Sec. II. The geometry of the thermoacoustic device was informed by the linear stability model of Migliorino and Scalo (2020b) with the goal of maximizing growth rate. Next, experimental results are presented in Sec. III. This includes a discussion of the typical waveform and temperature gradient behavior, results of parametric variation in base pressure, P_0 , and ΔT , and results of variation in resonator length. A comparison to numerical results is presented, along with description of the modeling approach, in Sec. IV. Finally, conclusions are summarized in Sec. V.

II. EXPERIMENTAL FACILITY

A. System overview

A schematic of the test apparatus is shown in Fig. 2, with dimensions given in Table I. A physical arrangement of the test article is shown in Fig. 3. Five 300 psid differential pressure transducers (P/N: PMP50E6-TD-A3-CA-H0-PG) (GE Druck, Leicester, UK) were installed along the resonator with one end attached to an isolation line for reference, allowing for higher accuracy than absolute transducers. Additionally, one absolute pressure measurement was taken on the test article in the hot side cavity using a Kulite pressure transducer (P/N: ETL-GTS-B-190-2000A) (Leonia, NJ), which was selected for its ability to withstand higher temperature limits while still maintaining a flush face with the interior of the wall. As the pressure amplitude in

the hot side cavity is the largest in the apparatus, all pressure amplitudes reported in this work were taken from this transducer unless stated otherwise. A second absolute pressure measurement was taken in Resonator Section 3 using a Unik 5000 (P/N: PMP50E6-TB-A3-CA-H0-PE-1000PSIA) (GE Druck, Leicester, UK).

Resonator Section 2 was constructed with multiple pieces of coiled stainless steel tubing, and sections of various tubing lengths were made which could be interchanged. The bend radius of the coils was 5.08 cm.

B. Thermal subsystem

The thermal diffusion ability is quantified by the thermal penetration depth, δ , which is the distance heat can diffuse into the working fluid during a fraction of the thermoacoustic period. δ is given by Eq. (3), where α_{th} is the thermal diffusivity, and ω is the angular acoustic frequency:

$$\delta = \sqrt{\frac{2\alpha_{th}}{\omega}} \tag{3}$$

Assuming the working fluid is being heated from all sides, it is desired to make the spacing where fluid absorbs

TABLE I. Lengths and internal diameters of test apparatus components (see Fig. 2).

| Component | Starting x loc. (cm) | Dia. (cm) |
|--------------|----------------------|-----------|
| Hot cavity | 0 | 2.35 |
| HHX | 5.08 | 2.35 |
| Stack | 7.11 | 2.35 |
| CHX | 13.2 | 2.35 |
| Res 1 | 15.2 | 2.35 |
| Res 2 | 20.3 | 0.46 |
| Res 3 | 224 | 10.7 |
| Res end wall | 239 | 10.7 |
| PT 1 | 1.65 | — |
| DPT 2 | 17.0 | — |
| DPT 3 | 47.5 | — |
| DPT 4 | 124 | — |
| DPT 5 | 200 | — |
| DPT 6 | 228 | — |
| PT 7 | 232 | — |
| TC 1 | 7.20 | — |
| TC2 | 9.13 | — |
| TC 3 | 11.1 | — |
| TC 4 | 13.0 | — |
| TC 5 | 14.9 | — |

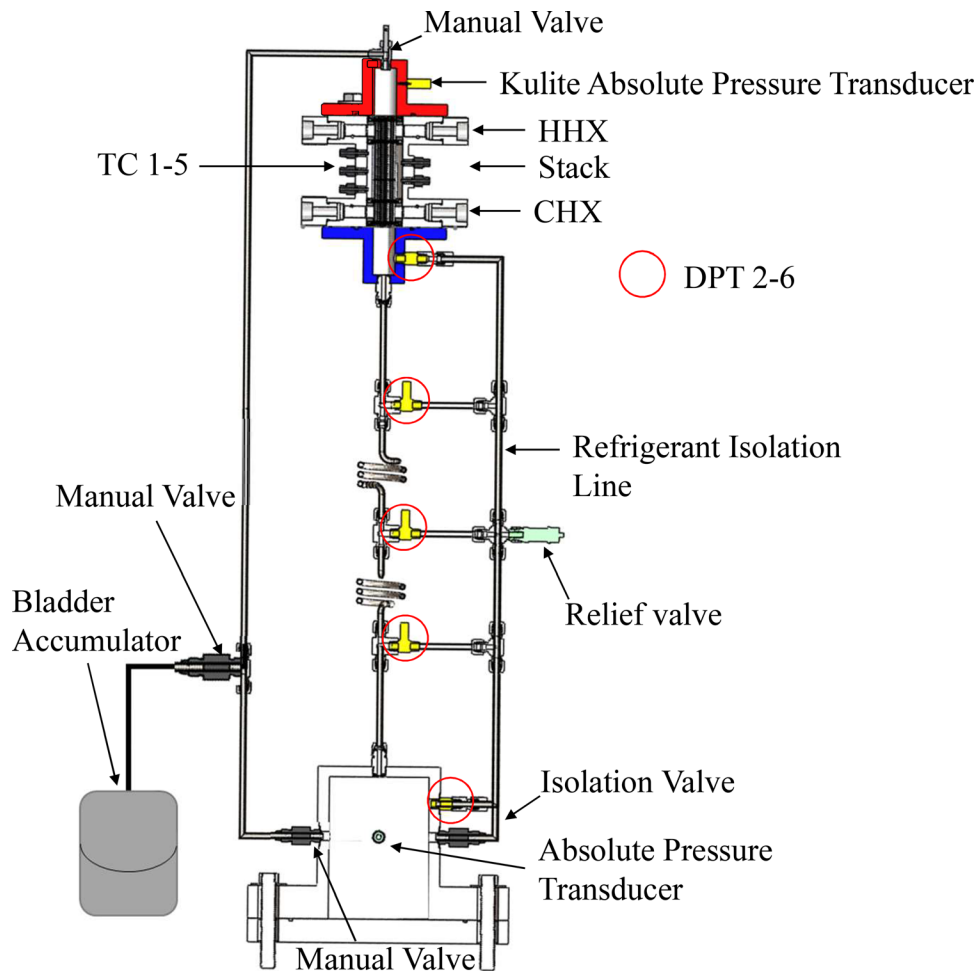


FIG. 3. (Color online) Physical arrangement of the test article.

and rejects heat equal to 2δ . Spacing larger than 2δ results in an inefficient diffusion of heat, while spacing smaller than 2δ can result in attenuation of the wave (Ceperley, 1979; Swift, 1988). Thus, the thermal penetration depth drives the design of the thermoacoustic stack.

Alexander (2018) performed experiments on various stack configurations with R-218, including honeycomb, metal foam, and microtube stacks. The microtube stack was the only configuration tested which generated a thermoacoustic oscillation, thus driving the design of the thermoacoustic stack to be made of microtubes for this work. A diagram of the thermal subsystem that contains the microtube stack is shown in Fig. 4.

The thermal subsystem consists of a stack of microtubes aligned in the axial direction inside of an aluminum shell. Refrigerant is allowed to flow axially through the microtubes, while heating and cooling fluids flow radially over the microtubes on either end of the stack. The hot and cold pathways are blocked off by four baffles, which allow for a temperature gradient to form in the region between the hot and cold ends. The volume surrounding the tubes was evacuated to limit heat transfer to axial conduction along the microtubes.

Type-K thermocouples were used to measure the incoming heating and cooling fluid temperatures, and ΔT

values reported in this manuscript are the difference in temperature measurements of these two thermocouples, averaged over the steady state period of data collection. Thermocouples were secured with compression fittings such that the tip of the thermocouple was in the center of the flow. Temperature measurements on the outgoing heating and cooling fluid flows were initially taken for the purpose of measuring efficiency. However, temperature drops across the heat exchangers only reach 2–4 K, and as the uncertainty of thermocouples is $\pm 2.2K$, efficiency cannot be reported in this manuscript. Additionally, five thermocouples were placed flush against the microtube stack with uniform axial spacing of 1.93 cm to assess the temperature gradient (see Fig. 4).

The porosity is a major design parameter of the stack design and is defined as the ratio of the cross sectional area of the working fluid to the total cross-sectional area of the stack. The microtubes are stainless steel and have an outer diameter of 0.3124 mm (0.0123") and an inner diameter of 0.2108 mm (0.0083"). The maximum porosity achievable was 12.3% (1530 microtubes), and this was limited by machinability constraints.

Assuming a 5 Hz frequency, R-218 has a penetration depth of approximately $13.7 \mu\text{m}$. Two times this penetration

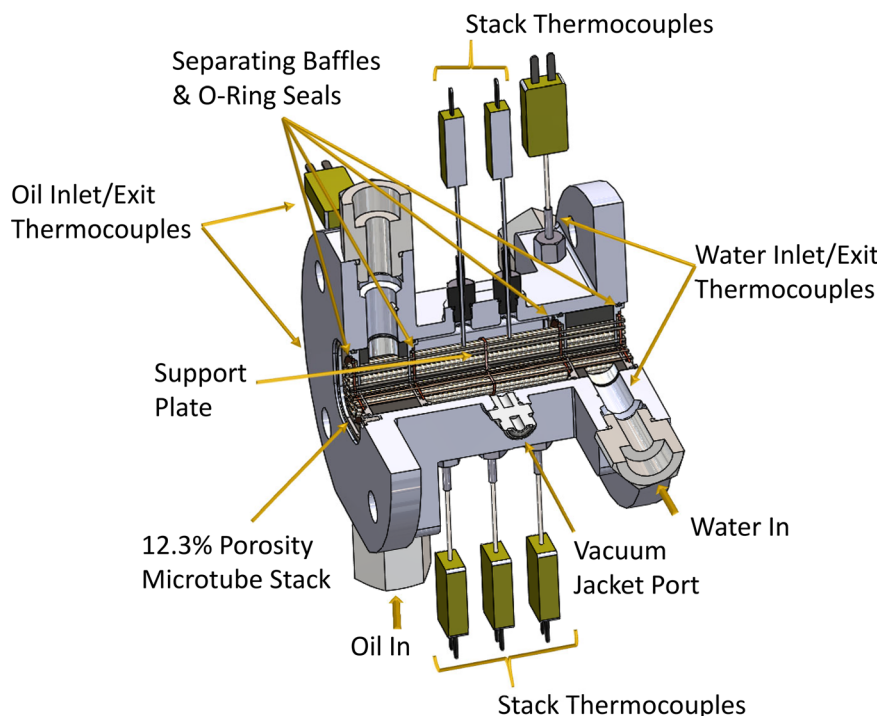


FIG. 4. (Color online) Internal view of thermal subsystem used in test campaign. Microtube bundle is 12.0 cm long and 2.35 cm in diameter.

depth is smaller than the manufacturing capabilities for a microtube heat exchanger. Increasing the thermal penetration depth would thus require a longer resonator to reduce the frequency, and this leads to a trade-off between increasing thermal penetration depth and increasing viscous losses, which will be discussed in Sec. III C.

Duratherm G (Tonowanda, NY) heat transfer oil was used as the heating fluid and ambient temperature filtered tap water was used as the cooling fluid. Both fluids flowed at approximately 3.8 L/min. Because R-218 is a greenhouse gas that requires containment, the fluid was pumped between the test article and a reclamation tank in a closed fluid circuit between tests. Data were collected using an NI Max (National Instruments, Austin, TX) data acquisition system where steady state data were collected for approximately 150 s. Pressure measurements were collected at 2000 Hz and temperature measurements were collected at 80 Hz.

III. EXPERIMENTAL RESULTS

The test campaign was divided into two major sets of tests: (1) variation of base pressure and ΔT and (2) variation of resonator length. Tables containing a complete list of test conditions are listed in the Appendix. For set 1, base pressure was varied between 0.9–1.3 P_{cr} , and ΔT was varied by maintaining the coolant at constant ambient temperature while changing the heating fluid between 373–444 K. For set 2, all geometry was kept the same except for Resonator Section 2, which was varied in length between 107–203 cm. ΔT was maintained at 116 K, and base pressure was varied between 1.05–1.2 P_{cr} for this set of tests.

Two examples of a typical waveform are shown in Fig. 5. When a sufficient temperature difference is imposed on the stack, the thermoacoustic instability appears

spontaneously, and the pressure amplitude grows exponentially until minor and other nonlinear losses counteracting the exponential growth leave the fluid at a limit-cycle amplitude. The minimum temperature difference required for thermoacoustic instabilities was observed to be approximately 75 K. The differences in the growth rate behaviors demonstrate that variations in the base pressure are affecting the thermal expansion of the fluid. We see that for the two compared tests, Test 53 has a much more rapid growth rate than Test 29. This is because, despite having a lower available thermal energy, Test 53 is closer to the critical point which means the fluid will have a larger thermal expansion coefficient and a steeper temperature gradient.

The thermoacoustic oscillation frequency was determined by applying a fast Fourier transform (FFT) to the raw data taken by each pressure transducer. To obtain the pressure amplitudes, the raw data were put through a second order low pass Butterworth filter with the frequency range set between 0.5 and 1.5 times the peak frequency determined by the FFT. The pressure amplitude was then averaged over the entire steady state interval. The uncertainty on the Kulite is $\pm 0.1\%$ of full scale output (± 20.7 kPa), and the uncertainties on the differential pressure transducers are $\pm 0.04\%$ of full scale output (± 0.827 kPa). A detailed uncertainty analysis of the data can be found in Martinez (2019).

The typical axial pressure profile inside the resonator can be seen in Fig. 6. Thermal energy is supplied to the left-hand side of the setup, and as the gas expands, it acts as a pump to accelerate the fluid in the resonator. Due to the smaller volume of the left-end cavity, compared to the right-end cavity, the pressure on this side is the highest. Fluid further from the stack is able to achieve higher velocities and thus a lower pressure amplitude, until the fluid hits the end wall and stagnates, causing the pressure amplitude to rise again.

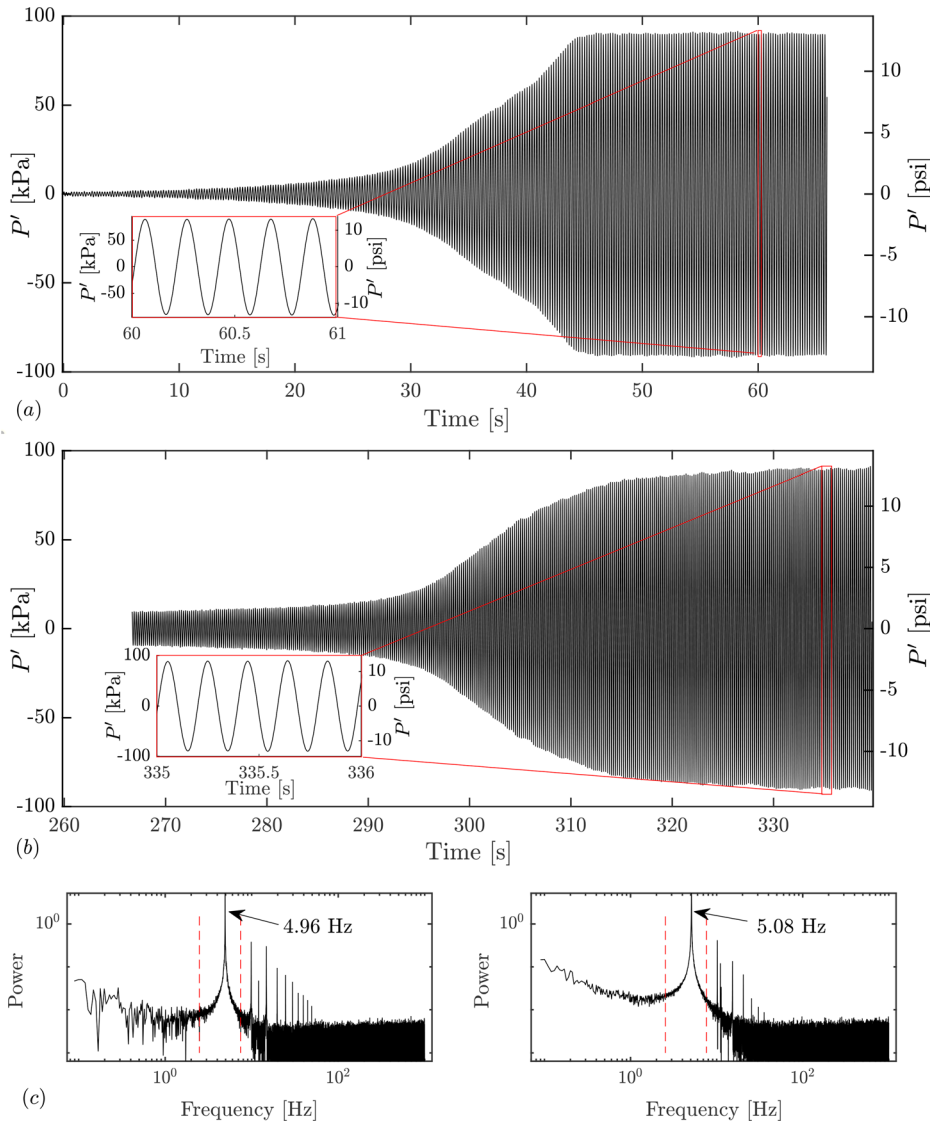


FIG. 5. (Color online) Typical waveform of bandpass-filtered data obtained in hot side cavity. Two examples are shown: (a) Test 53 operating at a ΔT of 79 K and a base pressure of $1.13 P_{cr}$ and (b) Test 29 operating at a ΔT of 87 K and a base pressure of $1.22 P_{cr}$. A constant temperature gradient imposed on the fluid creates spontaneous thermoacoustic instability that increases exponentially to a limit-cycle amplitude. The inset figures show zoomed-in limit-cycle oscillations of the region highlighted in red. (c) The power spectral density plots obtained from the raw data, with Test 53 on the left and Test 29 on the right. The red dashed lines mark the frequency range that was considered in the bandpass filter.

A. Variance of base pressure and ΔT

Thirty-five tests were conducted at steady state conditions in which the base pressure was varied from $0.9\text{--}1.3 P_{cr}$ ($2.38\text{--}3.43$ MPa), and ΔT was varied from 79–150 K.

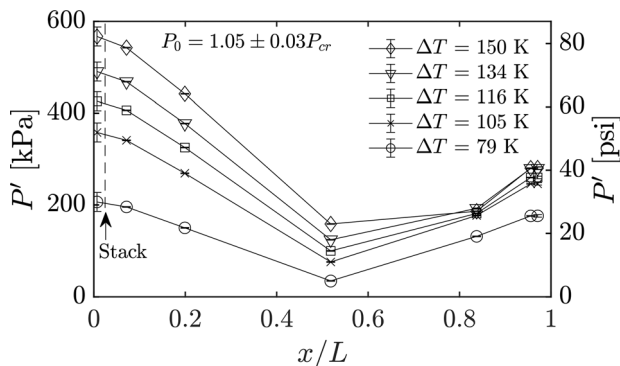


FIG. 6. Experimental pressure amplitude profile along the resonator for test numbers 5 225 354 258 (from lowest to highest ΔT).

Figure 7 shows the experimental results for frequency and pressure amplitude as a function of base pressure and temperature difference. The maximum pressure amplitude achieved was 669 kPa (97 psi) at a base pressure of $1.28 P_{cr}$ and ΔT of 150 K. The dominant frequency observed in all tests was between 4.7 and 6.2 Hz. The frequency is dictated by the sound speed of the fluid, the length of the resonator, and the diameter of the resonator. Because the vast majority of the fluid was held in the resonator section and remained as a pseudo-liquid at room temperature (giving it low compressibility), the operating frequency changed very little when ΔT and base pressure were varied. Figure 7(a) shows that pressure amplitude is a weak function of base pressure and is mostly dictated by the available thermal energy, presented as ΔT .

We see that a peak amplitude exists, and as ΔT increases, the base pressure at which this peak amplitude occurs moves away from the critical point. This is expected (Migliorino and Scalo, 2020b) because viscous losses counteract the high thermal expansion at the critical point.

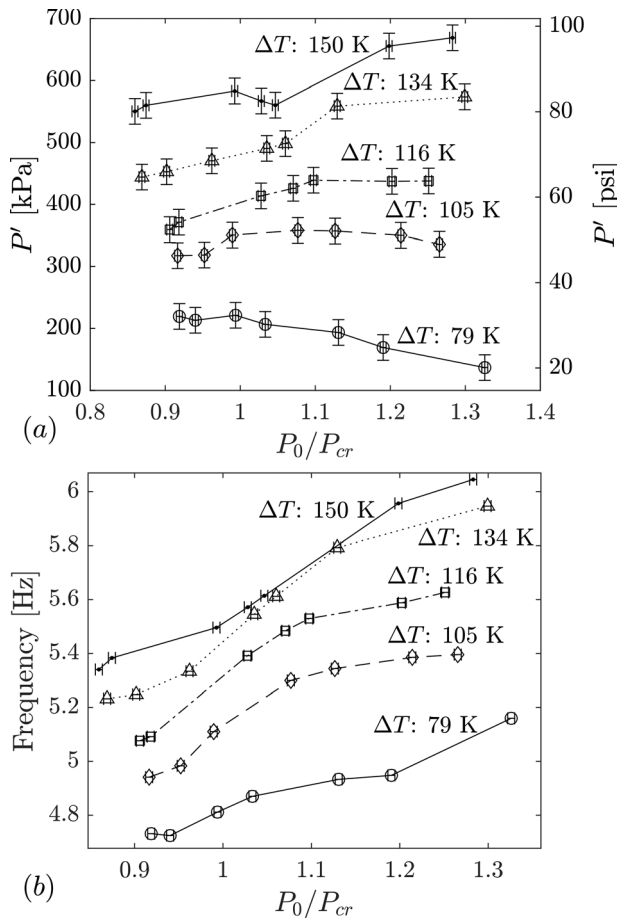


FIG. 7. Experimental results showing plots of thermoacoustic behavior with varying P_0 and ΔT . (a) amplitude and (b) frequency.

Increasingly nonlinear behavior of the waveform is observed with increasing ΔT . Migliorino and Scalo (2020a) give criteria for acoustic waves entering the nonlinear regime. In an acoustic device, the base density times the square of the sound speed, $\rho_0 a_0^2$, can be used as an estimate of the pressure amplitude limit for nonlinear wave propagation, P'_{nl} . The ratio, P'/P'_{nl} can then be used to classify the linearity of the wave propagation, where a ratio on the order of 10^{-7} is indicative of a perfectly linear acoustic wave, and a ratio on the order of 10^1 is a shock wave.

When we apply this analysis to the conditions present in the current study, $\rho_0 a_0^2$ is approximately 162 MPa, making the ratio P'/P'_{nl} approximately 10^{-3} . This puts the acoustic wave on the high end of the linear regime, where slight deviations from linear acoustic behavior can be expected, and indeed this behavior is observed. Figure 8 shows the pressure traces inside the resonator for a low-amplitude test condition [Fig. 8(a)] and a high-amplitude test condition [Fig. 8(b)]. The raw data subtracted by its average is plotted with the bandpass-filtered data, and it can be seen by the deviations in the two curves that wave steepening is becoming increasingly evident as the pressure amplitude increases. This is especially prominent in the pressure trace of DPT 4, where the fluid velocity is the highest.

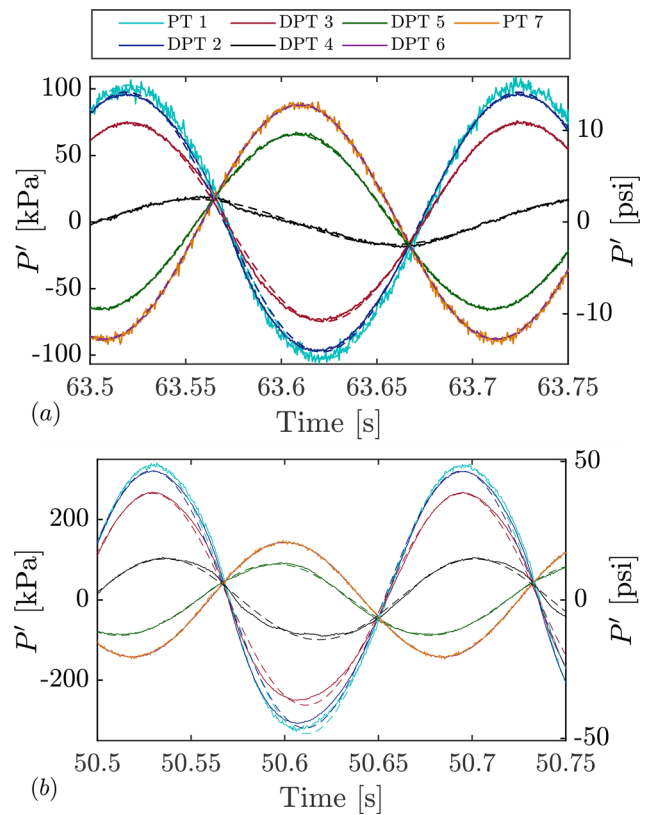


FIG. 8. (Color online) Pressure traces inside the resonator for (a) Test 52, conducted at $1.03 P_{cr}$ and ΔT of 79 K, and (b) Test 60, conducted at $1.28 P_{cr}$ and ΔT of 150 K. Solid lines show raw data subtracted by its average while dashed lines of equivalent color show the bandpass filtered pressure trace. Comparison of these charts show increased nonlinear behavior as the pressure amplitude increases. This is evidenced by wave-steepening that is seen as the raw data begin to deviate from the bandpass-filtered curve. This is most notably evident in the pressure trace of DPT 4, where the fluid velocity is the highest.

B. Temperature gradient profile

The temperature gradient consistently appears to be nonlinear in the subcritical region, and then takes on a more linear profile in the supercritical region. This is demonstrated in Fig. 9, which shows the temperature profile along the stack at three different base pressures and two different ΔT s. The reason for this is likely because a distinct phase-change process is occurring in the stack when the fluid is in the subcritical pressure regime. It is inferred that the fluid is boiling and creating vapor bubbles that travel upwards and carry heat with them sporadically. In the supercritical pressure regime, no distinct boundary occurs, and the temperature distribution is allowed to be more even.

This has interesting implications on the performance of the device, as it would suggest that in addition to the benefits of increased thermal expansion, the performance will be higher when the base pressure is supercritical due to the lack of vaporization enthalpy, leading to an increased ability for an even distribution of heat to occur.

We can see in Fig. 7(a) that for ΔT s of 150–105 K, the performance is highest when the base pressure is in the supercritical regime. However, the same trend is not

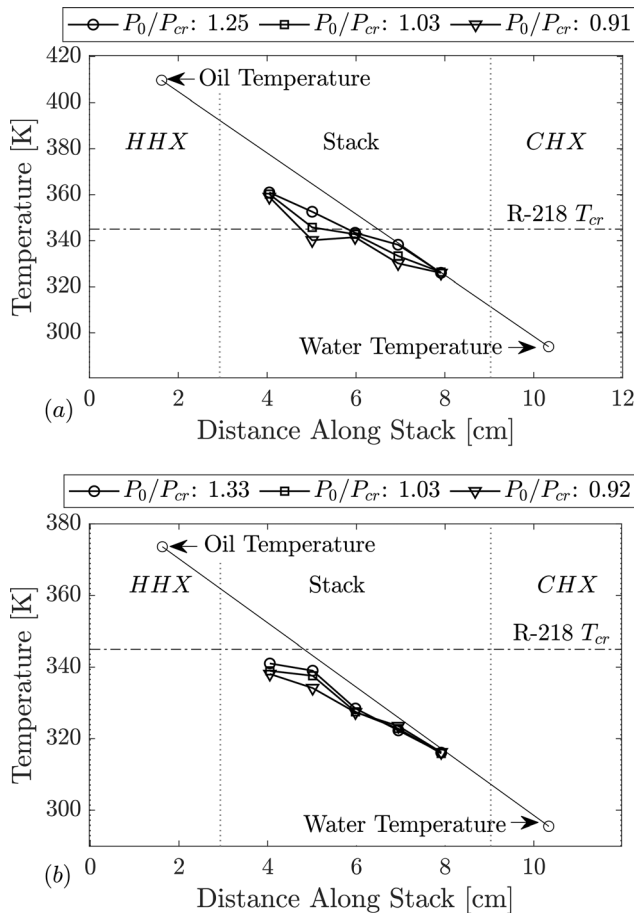


FIG. 9. Time-averaged temperature data obtained from thermocouple probes at evenly spaced locations along the stack at various base pressures for (a) $\Delta T = 116$ K and (b) $\Delta T = 79$ K.

observed for $\Delta T = 79$ K, where it is seen that the pressure amplitude is the highest in the subcritical pressure range, and decreases as base pressure increases. This can be explained by looking at Fig. 9(b). The maximum temperature measured in the stack hovers just below the critical temperature (345 K). The thermal barrier caused by the spike in heat capacity near the critical point makes it likely that although a hot side temperature well above the critical

temperature is imposed, the vast majority of the fluid in the stack is still below the critical temperature. Thus, the increased pressure in this temperature range would act as a hindrance to the gas expansion, as opposed to a benefit.

C. Variance of resonator length

Fifteen tests were conducted at steady state in which the resonator length was varied between 203 and 102 cm at three different base pressures. The resulting pressure amplitude and frequency with varying resonator length is shown in Fig. 10.

For all base pressures, the pressure amplitude increases as the resonator length increases, up to a peak at 178 cm, where pressure amplitude then begins to drop again. It is inferred that this trend is observed because as the resonator length increases, the frequency is lowered, allowing for more thermal diffusion time in the stack, thus increasing the pressure amplitude. The pressure amplitude peaks at 178 cm because as the resonator length increases, the viscous losses also increase. The amplitude peaks because the viscous losses incurred become greater than the benefits of increased thermal diffusion time. It is noted that as the resonator length increases, the length of coiled tubing also increases. Thus, increased viscous losses come from more wall friction as well as more flow turning.

The pressure amplitudes reported in Fig. 10 were measured with DPT 2 in Resonator Section 1, as opposed to PT 1, as is used for Fig. 7. This is because the increased accuracy of the differential transducer allows for a more confident observation of trends.

IV. MODELING APPROACH AND RESULTS

The modeling approach is based on the solution of the linearized Navier–Stokes equations and has been described in detail in previous works (Gupta *et al.*, 2017; Lin *et al.*, 2016; Migliorino and Scalo, 2020b). The numerical solution is obtained with a shift-Arnoldi algorithm, after discretizing the equations on a staggered uniform grid with second-order numerical operators. The model has been validated against results from direct numerical simulations of a standing-

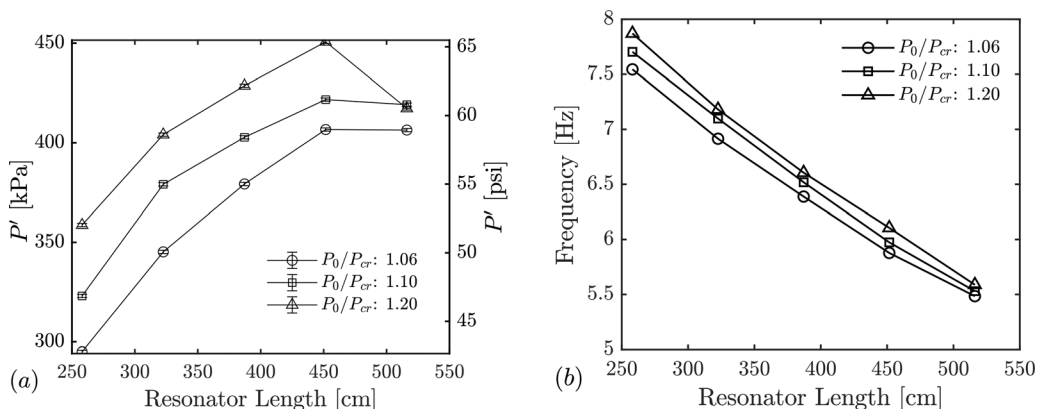


FIG. 10. Experimental results showing plots of thermoacoustic behavior with varying resonator length at a constant ΔT of 116 K. Transducer used is DPT-TA-02. (a) pressure amplitude with varying resonator length, (b) frequency with varying resonator length.

wave thermoacoustic minimal unit (Migliorino and Scalo, 2020b). This fast computational approach allows for the acoustic information of the system in the linear regime (such as growth rate, frequency, and eigenmodes) to be obtained, and is also able to model limit cycle physics, as discussed in the current section. In this work, the numerical solution is limited only to the first mode of fluid is considered at a uniform P_0 . On the right of the stack, a uniform base temperature equal to T_{cold} is imposed, while on its left, the base temperature is equal to T_{hot} . Inside of the stack, a linear temperature profile between T_{hot} and T_{cold} is imposed. The thermodynamic and transport properties of the base state are obtained from the Peng–Robinson equation of state (Peng and Robinson, 1976) and Chung’s model (Chung *et al.*, 1988), respectively.

A grid convergence study (see Fig. 11) allows us to choose $N=200$ as the number of pressure points which ensures an error of less than 0.5% on both growth rate and frequency. Tests with higher ΔT are less stringent in terms of required grid resolution.

The numerical approach is able to compute limit cycle pressure amplitudes by considering linearized pressure drops occurring at area changes or at coils, which can be

parametrized as (Idelchik, 1994; Lin *et al.*, 2016; Migliorino and Scalo, 2020b)

$$\Delta \hat{p} = -\beta \frac{K}{2} \rho_0 \frac{\hat{U}|\hat{U}|_{\text{lc}}}{A^2}, \quad (4)$$

where \hat{U} is the volumetric flow rate, ρ_0 is the fluid’s base state density, A is the smaller area, and K depends on the Reynolds number and on the ratio of the two duct areas or on coil’s geometrical parameters (Idelchik, 1994; Migliorino and Scalo, 2020b). The variable β is a tuning parameter which in this study, has been chosen equal to $\beta = 1.5$ in order to best fit the experimental data. The values of $|\hat{U}|$ at limit cycle, $|\hat{U}|_{\text{lc}}$, which are different for each area jump, are computed iteratively until a zero growth rate is obtained.

A comparison between numerical and experimental results for the supercritical tests in dataset 1 shows that errors are (for most tests) less than 10 and 15% for frequency and pressure amplitudes, respectively (Fig. 12). Error in pressure amplitude is the largest at the lowest ΔT , and this may be attributed to uncertainty in the true fluid

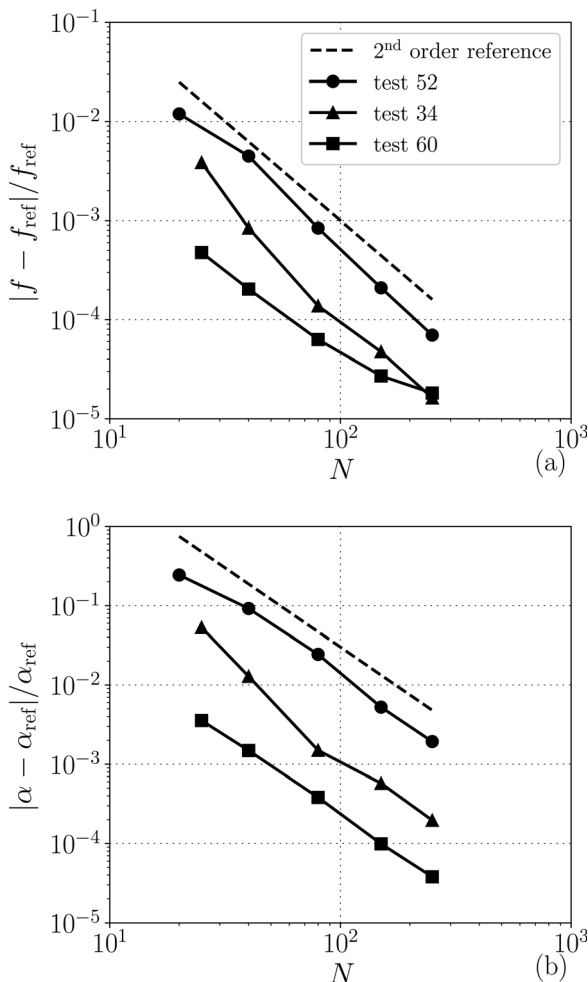


FIG. 11. Grid convergence analysis on frequency (a) and growth rate (b). Reference quantities are obtained with $N = 1000$.

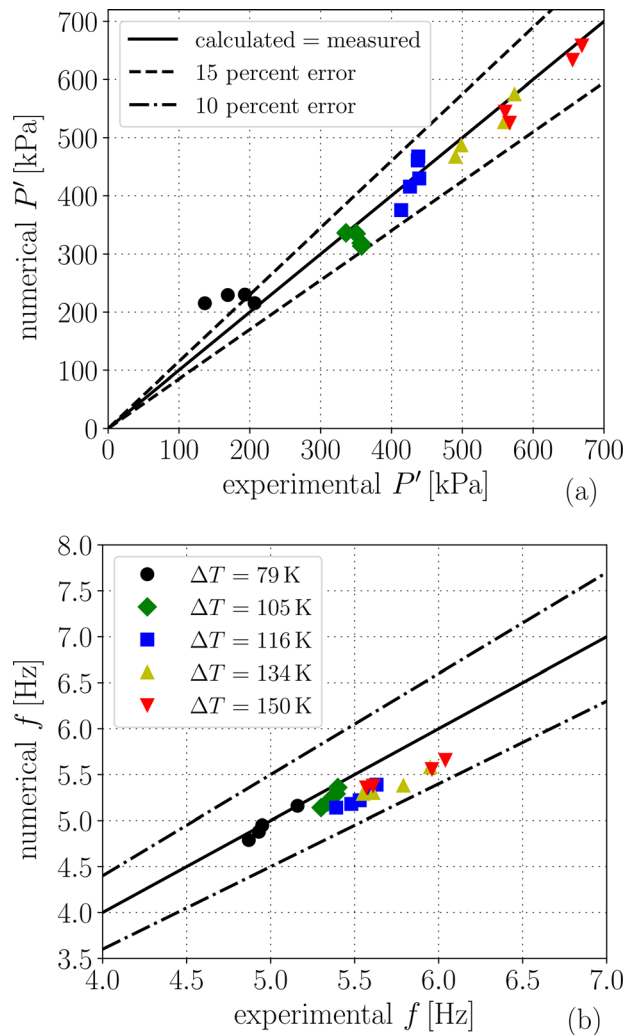


FIG. 12. (Color online) Comparison of experimental and numerical results for (a) pressure amplitude and (b) frequency for supercritical tests in Table II.

temperature. Sufficient evidence exists that because of the thermal barrier occurring near the critical point, the fluid never truly reaches its critical temperature at the lowest ΔT .

While the prediction of the frequency is not very sensitive to the value of β , the pressure amplitudes obtained from the model strongly depend on it, since β primarily influences the value of the pressure losses that are responsible for the linearized limit cycle obtained. Numerical results on frequency show the best agreement for low values of ΔT , indicating that at higher pressure amplitudes other effects not taken into account, such as nonlinear wave steepening, might have a relevant role.

The numerical pressure profiles along the resonator (Fig. 13), if compared to the experimental ones at the same conditions (Fig. 6), are in good qualitative agreement. The model shows limit cycle pressure drops at area changes and coils locations, and a flat pressure in the resonator 3 section as observed in the experiments.

The acoustic power (in watts) produced by the stack, obtained as the difference between the acoustic power at the beginning of resonator 1 and at the beginning of the hot cavity, can be approximated by the relation

$$W_{\text{stk}} = 0.11P'^2, \tag{5}$$

where P' is the maximum peak-to-peak pressure amplitude measured in the bar (see Fig. 14).

V. CONCLUSION

The goal of this research was to characterize the thermoacoustic response of transcritical R-218, as transcritical fluids with high density gradients and high thermal expansion coefficients have the potential to produce higher power outputs in thermoacoustic devices than traditional ideal gas working fluids, and can work with milder temperature gradients.

The thermoacoustic response was characterized at seven different base pressures, ranging from 0.9–1.3 P_{cr} and five different ΔT s, ranging from 79–150 K. This characterization

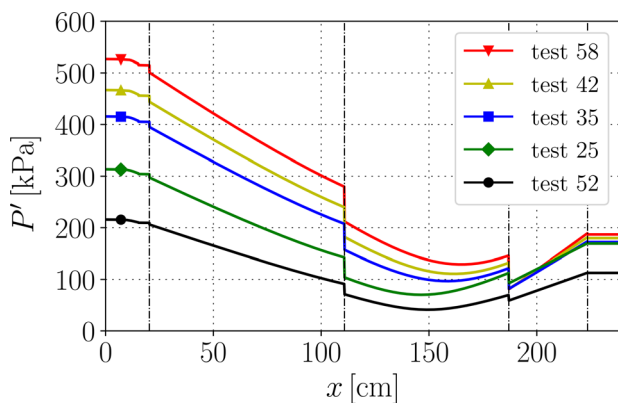


FIG. 13. (Color online) Numerical pressure amplitude profile along the resonator for test numbers 5 225 354 258. Vertical dashed lines indicate ending locations of resonator 1, coiled sections, and resonator 2.

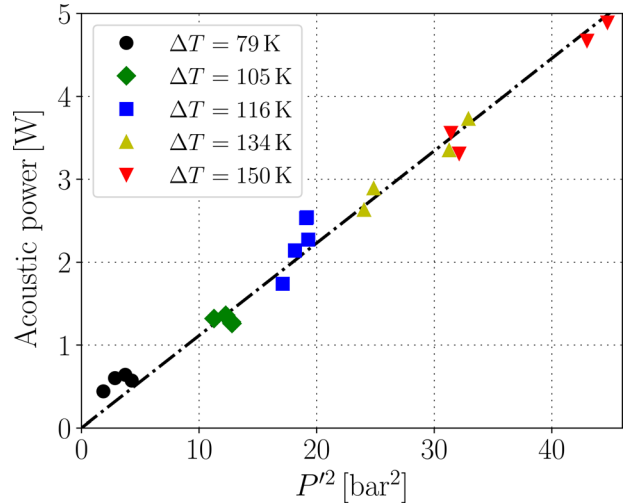


FIG. 14. (Color online) Numerical acoustic power produced by the stack versus numerical peak-to-peak maximum pressure amplitude squared for supercritical tests in Table II.

was done in a closed apparatus without any energy extraction, and the highest pressure amplitude achieved was 669 kPa at a frequency of 6.04 Hz. Overall, the amplitude of the instability grew with increased input energy as inferred by ΔT supplied to the thermoacoustic stack. For a given resonator configuration, the frequency of the instability varied only about 28% over the pressure and temperature ranges studied.

Additionally, the effect of resonator length on the thermoacoustic response was characterized. The thermoacoustic response was measured at five different resonator lengths varying from 100–200 cm at three different base pressures. The results of these tests demonstrated that the pressure amplitude was maximized at a resonator length of 179 cm. The reason for this is that the increased resonator length decreased the frequency, allowing for a longer thermal diffusion time inside the stack. It is presumed that the amplitude peaked at the point where viscous losses in the resonator outweighed the benefit of lowered frequency.

The experimental results were compared to numerical predictions which show fair agreement. Percent error in pressure amplitude predictions decreases as the thermal energy supply increases, which ensures a transcritical state inside the stack. In contrast, the model tends to slightly underpredict the operating frequency and has the best agreement when the thermal energy supply is the lowest, due to increased nonlinear losses occurring at the higher pressure amplitudes. Differences in numerical predictions may be affected by uncertainty in the true fluid temperature caused by thermal barrier effects around the critical point, and modeling uncertainties for pressure losses at area jumps and coils for oscillating flow.

Based on the findings detailed, work has been continued on this test apparatus to investigate the effects of changing resonator diameter and removing coils. Results of these

investigations are detailed in [Martinez et al. \(2021\)](#), and are outside the scope of discussion for the current manuscript.

ACKNOWLEDGMENTS

This work has been funded by Rolls-Royce Corporation Indianapolis. The guidance of Patrick C. Sweeney is gratefully acknowledged. M.T.M. also acknowledges the support of the Frederick N. Andrews Doctoral Fellowship at Purdue University.

Conflict of Interest

The authors declare no conflict of interest.

APPENDIX

This section contains a complete list of relevant test conditions and test results (Tables II and III).

TABLE II. Experimental results of thermoacoustic behavior with varying base pressure and ΔT (dataset 1). For all tests, $L_{res2} = 203.2$ cm.

| Test | P_0/P_{cr} | ΔT (K) | P' (kPa) | f (Hz) |
|------|--------------|----------------|------------|----------|
| 48 | 0.92 | 78 | 219 | 4.73 |
| 49 | 0.94 | 78 | 213 | 4.72 |
| 51 | 0.99 | 79 | 221 | 4.81 |
| 52 | 1.03 | 79 | 207 | 4.87 |
| 53 | 1.13 | 79 | 193 | 4.93 |
| 54 | 1.19 | 79 | 169 | 4.95 |
| 55 | 1.33 | 79 | 137 | 5.16 |
| 29 | 1.22 | 87 | 196 | 5.08 |
| 22 | 0.92 | 105 | 317 | 4.94 |
| 23 | 0.95 | 105 | 319 | 4.98 |
| 24 | 0.99 | 106 | 351 | 5.11 |
| 25 | 1.08 | 105 | 358 | 5.30 |
| 26 | 1.13 | 105 | 357 | 5.34 |
| 27 | 1.21 | 106 | 350 | 5.39 |
| 28 | 1.27 | 106 | 336 | 5.40 |
| 32 | 0.91 | 116 | 359 | 5.08 |
| 38 | 0.92 | 116 | 371 | 5.09 |
| 33 | 1.03 | 116 | 414 | 5.39 |
| 35 | 1.07 | 116 | 426 | 5.48 |
| 34 | 1.10 | 116 | 439 | 5.53 |
| 36 | 1.20 | 116 | 437 | 5.59 |
| 37 | 1.25 | 116 | 438 | 5.63 |
| 39 | 0.87 | 134 | 444 | 5.23 |
| 40 | 0.90 | 134 | 453 | 5.25 |
| 41 | 0.96 | 134 | 470 | 5.33 |
| 42 | 1.04 | 134 | 491 | 5.55 |
| 43 | 1.06 | 134 | 498 | 5.61 |
| 44 | 1.13 | 134 | 559 | 5.79 |
| 45 | 1.30 | 134 | 574 | 5.95 |
| 46 | 0.86 | 151 | 550 | 5.34 |
| 47 | 0.87 | 151 | 560 | 5.38 |
| 52 | 1.03 | 79 | 207 | 4.87 |
| 56 | 0.99 | 150 | 583 | 5.50 |
| 58 | 1.03 | 150 | 567 | 5.57 |
| 57 | 1.05 | 150 | 560 | 5.61 |
| 59 | 1.20 | 150 | 656 | 5.96 |
| 60 | 1.28 | 150 | 669 | 6.04 |

TABLE III. Experimental results for dataset 2, aimed at assessing the impact of varying resonator length on thermoacoustic response. For all tests $\Delta T = 116$ K.

| Test No. | P_0/P_{cr} | L_{res2} (cm) | P' (kPa) | f (Hz) |
|----------|--------------|-----------------|------------|----------|
| 35 | 1.07 | 203 | 426 | 5.48 |
| 34 | 1.10 | 203 | 439 | 5.53 |
| 36 | 1.20 | 203 | 437 | 5.59 |
| 70 | 1.05 | 178 | 428 | 5.88 |
| 69 | 1.09 | 178 | 443 | 5.97 |
| 71 | 1.20 | 178 | 473 | 6.11 |
| 67 | 1.06 | 152 | 400 | 6.39 |
| 66 | 1.10 | 152 | 425 | 6.52 |
| 68 | 1.20 | 152 | 452 | 6.61 |
| 73 | 1.05 | 127 | 368 | 6.91 |
| 72 | 1.10 | 127 | 403 | 7.10 |
| 74 | 1.20 | 127 | 430 | 7.18 |
| 75 | 1.05 | 102 | 317 | 7.54 |
| 77 | 1.10 | 102 | 346 | 7.70 |
| 78 | 1.21 | 102 | 384 | 7.87 |

Adeff, J. A., Hofler, T. J., and Garrett, S. L. (1991). "A thermoacoustic refrigerator for space applications," *J. Acoust. Soc. Am.* **90**(4), 2304–2304.

Alexander, D. (2018). "Experimental study of a standing-wave transcritical thermoacoustic device," Master's thesis, Purdue University, West Lafayette, IN.

Alexander, D., Migliorino, M. T., Heister, S. D., and Scalo, C. (2018). "Numerical and experimental analysis of a transcritical thermoacoustic prototype," in *AIAA Aviation Forum, Fluid Dynamics Conference*, American Institute of Aeronautics and Astronautics, June 25–29, Atlanta, GA.

Backhaus, S., and Swift, G. W. (1999). "A thermoacoustic Stirling heat engine," *Nature* **399**(6734), 335–338.

Backhaus, S., and Swift, G. W. (2000). "A thermoacoustic-Stirling heat engine: Detailed study," *J. Acoust. Soc. Am.* **107**(6), 3148–3166.

Belcher, J. R., Slaton, W. V., Raspet, R., Bass, H. E., and Lightfoot, J. (1999). "Working gases in thermoacoustic engines," *J. Acoust. Soc. Am.* **105**(5), 2677–2684.

Ceperley, P. H. (1979). "A pistonless Stirling engine – The traveling wave heat engine," *J. Acoust. Soc. Am.* **66**(5), 1508–1513.

Chung, T.-H., Ajlan, M., Lee, L. L., and Starling, K. E. (1988). "Generalized multiparameter correlation for nonpolar and polar fluid transport properties," *Ind. Eng. Chem. Res.* **27**(4), 671–679.

de Blok, K., Owczarek, P., and Francois, M.-X. (2014). "Bi-Directional Turbines for Converting Acoustic Wave Power into Electricity," *9th PAMIR International Conference on Fundamental and Applied MHD*, 433–438.

Dong, S., Shen, G., Xu, M., Zhang, S., and An, L. (2019). "The effect of working fluid on the performance of a large-scale thermoacoustic Stirling engine," *Energy* **181**, 378–386.

Gupta, P., Lodato, G., and Scalo, C. (2017). "Spectral energy cascade in thermoacoustic shock waves," *J. Fluid Mech.* **831**, 358–393.

Hunt, S., and Heister, S. (2017). "Thermoacoustic oscillations in multipath heated fuel circuits," *J. Heat Transfer* **139**(9), 091801.

Idelchik, I. E. (1994). *Handbook of Hydraulic Resistance*, 3rd ed. (CRC Begell House).

Jin, T., Huang, J., Feng, Y., Yang, R., Tang, K., and Radebaugh, R. (2015). "Thermoacoustic prime movers and refrigerators: Thermally powered engines without moving components," *Energy* **93**, 828–853.

Lemmon, E. W., McLinden, M. O., and Friend, D. G. (2016). "69 Thermophysical properties of fluid systems," in *NIST Chemistry Webbook, NIST Standard Reference Database* (National Institute of Standards and Technology, Gaithersburg MD).

Li, D.-H., Chen, Y.-Y., Luo, E.-C., and Wu, Z.-H. (2014). "Study of a liquid-piston traveling-wave thermoacoustic heat engine with different working gases," *Energy* **74**, 158–163.

- Lin, J., Scalo, C., and Hesselink, L. (2016). "High-fidelity simulation of a standing-wave thermoacoustic-piezoelectric engine," *J. Fluid Mech.* **808**, 19–60.
- Malone, J. F. J. (1931). "A new prime mover," *J. R. Soc. Arts* **79**(4099), 679–709.
- Martinez, A. (2019). "Experimental Study of a Low-Frequency Thermoacoustic Device," Master's thesis, Purdue University, West Lafayette, IN.
- Martinez, A. G., Kuras, B., Tindaro Migliorino, M., Scalo, C., and Heister, S. D. (2021). "Experimental demonstration of high-amplitude thermoacoustic instabilities under transcritical temperature conditions in a standing-wave device," *AIAA Scitech* 2021 Forum, 1175.
- Migliori, A., and Swift, G. W. (1988). "Liquid-sodium thermoacoustic engine," *Appl. Phys. Lett.* **53**(5), 355–357.
- Migliorino, M. T., and Scalo, C. (2020a). "Heat-induced planar shock waves in supercritical fluids," *Shock Waves* **30**(2), 153–167.
- Migliorino, M. T., and Scalo, C. (2020b). "Real-fluid effects on standing-wave thermoacoustic instability," *J. Fluid Mech.* **883**, A23.
- Peng, D.-Y., and Robinson, D. B. (1976). "A new two-constant equation of state," *Ind. Eng. Chem. Fundam.* **15**(1), 59–64.
- Rayleigh, L. (1878). "The explanation of certain acoustical phenomena," *Nature* **18**, 319–321.
- Slaton, W. V., Rayburn, J. W., Hiller, R. A., and Raspet, R. (2001). "Reduced onset temperature difference in wet thermoacoustic engines," *J. Acoust. Soc. Am.* **110**(5), 2677–2678.
- Swift, G. W. (1988). "Thermoacoustic engines," *J. Acoust. Soc. Am.* **84**(4), 1145–1180.
- Tijani, M. E. H., and Spoelstra, S. (2011). "A high performance thermoacoustic engine," *J. Appl. Phys.* **110**(9), 093519–093519.
- Yazaki, T., Iwata, A., Maekawa, T., and Tominaga, A. (1998). "Traveling wave thermoacoustic engine in a looped tube," *Phys. Rev. Lett* **81**, 3128–3131.